Since January 2020 Elsevier has created a COVID-19 resource centre with free information in English and Mandarin on the novel coronavirus COVID-19. The COVID-19 resource centre is hosted on Elsevier Connect, the company's public news and information website.

Cell Reports

Article

Remdesivir overcomes the S861 roadblock in SARS-CoV-2 polymerase elongation complex

Graphical abstract

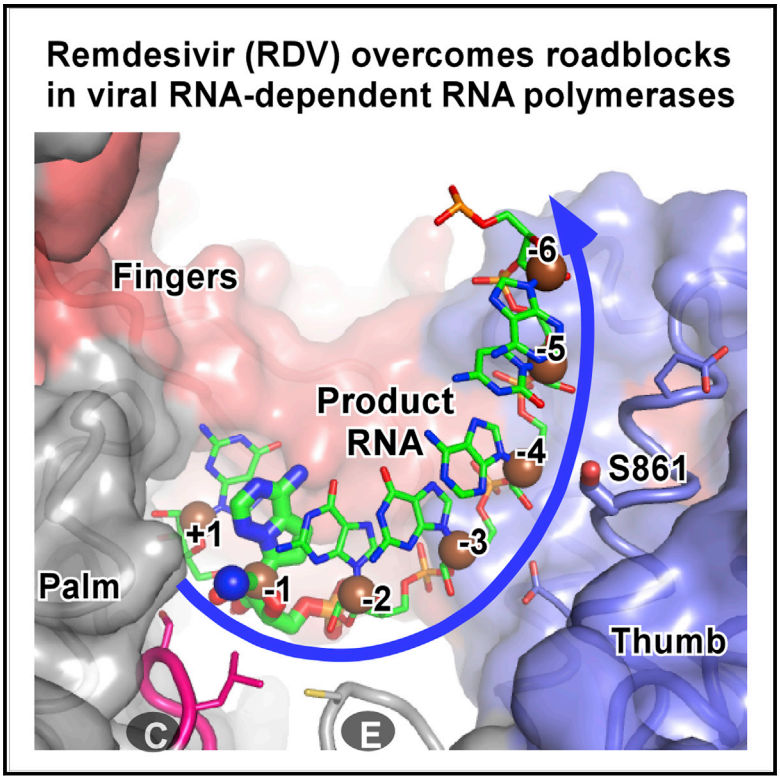

Highlights

- SARS-CoV-2 RdRP elongation complex assembled via multiple nucleotide addition cycles
- Remdesivir overcomes the S861 roadblock in the SARS-CoV-2 RdRP elongation complex
- Remdesivir induces delayed intervention at the equivalent site in EV71 RdRP
- Delayed intervention of RdRP by 1′-modified nucleotide analogs may generally occur

Authors

Jiqin Wu, Haofeng Wang, Qiaojie Liu, ..., Quan Wang, Zihe Rao, Peng Gong

Correspondence

wangq@shanghaitech.edu.cn (Q.W.), raozh@tsinghua.edu.cn (Z.R.), gongpeng@wh.iov.cn (P.G.)

In brief

Remdesivir (RDV), a drug effective in COVID-19 treatment, induces a characteristic delayed intervention once incorporated by the SARS-CoV-2 polymerase. Wu et al. reveal that RDV incorporated by SARS-CoV-2 polymerase elongation complex can pass the intervention site, while a similar mechanism is also found in enterovirus 71 polymerase.

Wu et al., 2021, Cell Reports 37, 109882
October 26, 2021
https://doi.org/10.1016/j.celrep.2021.109882

CellPress

Cell Reports

CellPress
OPEN ACCESS

Article

Remdesivir overcomes the S861 roadblock in SARS-CoV-2 polymerase elongation complex

Jiqin Wu,[1,8] Haofeng Wang,[2,8] Qiaojie Liu,[1,8] Rui Li,[1,3] Yan Gao,[4] Xiang Fang,[1,3] Yao Zhong,[1,3] Meihua Wang,[1,3] Quan Wang,[5,*] Zihe Rao,[4,5,6,*] and Peng Gong[1,7,9,*]

[1]Key Laboratory of Special Pathogens and Biosafety, Wuhan Institute of Virology, Center for Biosafety Mega-Science, Chinese Academy of Sciences, No. 44 Xiao Hong Shan, Wuhan, Hubei 430071, China
[2]School of Life Sciences, Tianjin University, Tianjin 300072, China
[3]University of Chinese Academy of Sciences, Beijing 100049, China
[4]Laboratory of Structural Biology, School of Life Sciences and School of Medicine, Tsinghua University, Beijing 100084, China
[5]Shanghai Institute for Advanced Immunochemical Studies and School of Life Science and Technology, ShanghaiTech University, Shanghai 201210, China
[6]National Laboratory of Biomacromolecules, CAS Center for Excellence in Biomacromolecules, Institute of Biophysics, CAS, Beijing 100101, China
[7]Drug Discovery Center for Infectious Diseases, Nankai University, Tianjin 300350, China
[8]These authors contributed equally
[9]Lead contact
*Correspondence: wangq@shanghaitech.edu.cn (Q.W.), raozh@tsinghua.edu.cn (Z.R.), gongpeng@wh.iov.cn (P.G.)
https://doi.org/10.1016/j.celrep.2021.109882

SUMMARY

Remdesivir (RDV), a nucleotide analog with broad-spectrum features, has exhibited effectiveness in COVID-19 treatment. However, the precise working mechanism of RDV when targeting the viral RNA-dependent RNA polymerase (RdRP) has not been fully elucidated. Here, we solve a 3.0-Å structure of severe acute respiratory syndrome coronavirus 2 (SARS-CoV-2) RdRP elongation complex (EC) and assess RDV intervention in polymerase elongation phase. Although RDV could induce an "i+3" delayed termination in meta-stable complexes, only pausing and subsequent elongation are observed in the EC. A comparative investigation using an enterovirus RdRP further confirms similar delayed intervention and demonstrates that steric hindrance of the RDV-characteristic 1′-cyano at the −4 position is responsible for the "i+3" intervention, although two representative *Flaviviridae* RdRPs do not exhibit similar behavior. A comparison of representative viral RdRP catalytic complex structures indicates that the product RNA backbone encounters highly conserved structural elements, highlighting the broad-spectrum intervention potential of 1′-modified nucleotide analogs in anti-RNA virus drug development.

INTRODUCTION

RNA viruses include numerous important human pathogens and have caused multiple epidemics of global concern in the past two decades. The coronavirus disease 2019 (COVID-19) causing a global pandemic is caused by an RNA virus, severe acute respiratory syndrome coronavirus 2 (SARS-CoV-2), belonging to the *Coronaviridae* of the *Nidovirales*. The RNA-dependent RNA polymerase (RdRP) is the only universal gene encoded by the RNA virus (Wolf et al., 2018), and the RdRP proteins play central roles in the DNA-independent genome replication and transcription processes essential for an RNA virus life cycle. Comparing with other classes of nucleic acid polymerase, the RdRPs exhibited unique features, including a palm-based conformational change leading to the pre-catalysis active site closure and a motif G-based stringent control of template strand movement during the post-catalysis translocation (Appleby et al., 2015; Gong and Peersen, 2010; Shu and Gong, 2016; Wang et al., 2020b; Zamyatkin et al., 2008). Therefore, viral RdRPs are ideal systems to study the RNA-only replication and to develop antiviral drugs for treatment of RNA virus-related diseases.

Nucleotide/nucleoside analogs (NAs) have become an important class of small molecule compounds targeting various types of polymerase, with the most common effective form being their nucleoside triphosphate (NTP) metabolites (De Clercq and Li, 2016; Jordheim et al., 2013). To date, the most successful NA for treatment of RNA virus-related diseases is sofosbuvir (SOF), a ribose 2′-modified uridine analog, that has played a key role in prevention and control of hepatitis C (Gane et al., 2013, 2014). Despite its high effectiveness against hepatitis C virus (HCV), this compound has not been proved to be clinically effective for treatment of diseases caused by other important RNA viruses. Another representative NA drug favipiravir (FVP), a base analog capable of base pairing with cytosine (C) or uracil (U) bases, was first developed to treat influenza and has shown a broad-spectrum effect against other RNA viruses, including SARS-CoV-2 (Du and Chen, 2020; Furuta et al., 2013; Wang et al., 2020a). Similar to the classical broad-spectrum NA

ribavirin (RBV), FVP is believed to act as a mutagen in RNA replication through its non-rigorous base-pairing property, while a higher-than-necessary mutation rate in RNA virus replication can lead to error catastrophe and virus extinction (Crotty et al., 2001; Pfeiffer and Kirkegaard, 2003). However, SOF and FVP may have been the only clinically successful NA drugs applicable to limited RNA virus-related diseases. Therefore, development of either highly effective or potent broad-spectrum NA drugs against important RNA viruses has become an urgent need.

Remdesivir (RDV) is an NA with a characteristic modification at the ribose 1′-position. It was first developed against Ebola virus (EBoV) and entered clinical trials during recent Ebola epidemics in Africa (Jacobs et al., 2016). It has been shown to be effective against several CoVs and therefore was immediately tested in searching for SARS-CoV-2 drug candidates (Wang et al., 2020a). Although RDV has been approved by the European Union and the United States for COVID-19 treatment, data derived from clinical trials suggest that its effectiveness is not ideal (Beigel et al., 2020; Goldman et al., 2020). Hence understanding its precise intervention and broad-spectrum mechanism and further optimizing its antiviral activity through rational design will benefit the development of NA drugs against clinically important RNA viruses in general. As an adenosine analog, the NTP form of RDV (RDV-TP) has been shown to have comparable or higher reactivity than ATP in uridine (U)-directed RdRP synthesis (Gordon et al., 2020; Tchesnokov et al., 2019; Wang et al., 2020c). Unlike classical chain terminators, RDV typically does not induce immediate-chain termination once incorporated. Recent studies characterizing RDV-TP intervention on SARS-CoV-2 RdRP demonstrated that RDV could induce a delayed termination three catalytic events after its incorporation (“i+3” termination), while a similar mechanism was not observed in EBoV RdRP (Gordon et al., 2020). Structural analysis and enzymology characterization further highlight the involvement of a thumb domain residue, S861, in inducing this delayed intervention presumably through a steric clash with the 1′-cyano group of RDV (Gordon et al., 2020; Tchesnokov et al., 2020; Wang et al., 2020c). In this work, by assembling SARS-CoV-2 RdRP catalytic complexes at distinct stability levels, we are able to assess and compare the intervention mechanisms of RDV both in a meta-stable complex and a *bona fide* elongation complex (EC). Although an RDV-induced delayed termination was evident in the meta-stable complex, RDV caused only temporal pausing in the EC. By solving a cryo-electron microscopy (cryo-EM) structure of SARS-CoV-2 RdRP EC, we were able to identify critical interactions and conformational changes contributing to EC stability, and this EC system may help future efforts in direct observation of the proposed steric clash. Through comparative analyses of catalytic complex structures from representative RdRPs, we proposed a general RdRP intervention mechanism for RDV that may benefit future development of potent NA drugs against RNA viruses.

RESULTS

RDV represents a unique NA type in RdRP intervention

Chain-terminating NAs have exhibited potency in various polymerase systems (Elion et al., 1977; Hakimelahi et al., 2001). Classical chain terminators such as the anti-herpetic drug acyclovir (ACV) do not contain a 3′-hydroxyl group and will not allow further catalysis after the incorporation of its nucleoside monophosphate (NMP) form (Tchesnokov et al., 2009). Some 2′-modified NAs, including SOF, exhibited similar behaviors in RdRP intervention, although the presence of 3′-hydroxyl theoretically allows further extension (Potisopon et al., 2017; Xu et al., 2017). Here, we compared the properties of the NTP form of SOF (SOF-TP) with UTP in a primer-dependent RdRP assay using SARS-CoV-2 nsp12-nsp7-nsp8 and a T33-8/P10 RNA construct comprising a 33-mer template (T33) and a 10-mer primer (P10) (Figure 1A). In the presence of C, U, and ATP (C/U/A), the P10 can be readily converted to a 17-mer product (P17) within 60 min (Figure 1A, lanes 2–4 and 12–14). When UTP was replaced by SOF-TP (C/S/A), P10 conversion was as efficient, but a very low level of extension (indicated by the amount of P17) occurred after the incorporation of SOF (Figure 1A, lanes 5–7 and 15–17; for simplicity, NA abbrieviations are used to indicate their NMP form incorporated by RdRP), suggesting that SOF may act as a nonobligate chain terminator in SARS-CoV-2 RdRP replication (Lu et al., 2020). We next tested T-1105, a structural analog of FVP, in a similar assay using a T35/P10 construct (Figure 1B). Comparing with incorporation in the presence of G and ATP (G/A), either the combination of GTP and the NTP form of T-1105 (T-1105-TP) (G/t) or ATP and T-1105-TP (A/t) led to faster conversion of P10 to a 16-mer product (P16). These observations suggest that T-1105-TP is able to efficiently mimic GTP or ATP and could allow further extension after incorporation (Figure 1B), consistent with previous reports in characterizing FVP intervention on viral RdRPs (Jin et al., 2013, 2015). Different from the interventions brought by SOF and T-1105, incorporation of RDV led to appearance of the “i+3” 15-mer product (P15) on a T33-1/P10 construct (Gordon et al., 2020; Wang et al., 2020c) (Figure 1C, lanes 45–47 and 55–57). This delayed intervention mechanism is different from either traditional chain termination represented by ACV and SOF or non-terminating mechanism by RBV and FVP/T-1105.

We previously solved an RDV-containing SARS-CoV-2 RdRP catalytic complex using a T33-7/P10 construct (Wang et al., 2020c). Somewhat unexpectedly, an “i+1” 18-mer product (P18) was observed in this complex likely because of both interactions between the downstream stem-loop RNA region and nsp12 and the incorporation of RDV. These RNA sequence/local structure-dependent interactions probably induced a pausing at this particular stage and trapped the RdRP in a pre-translocation state. In a gel-based assessment, “i+3” product was also observed and accompanied by extension of the “i+1” product, demonstrating the pausing nature of the latter, while by contrast, this “i+1” product was not prominent in regular NTP-driven reactions (Wang et al., 2020c). Here, we increased the reaction duration to 4 h (versus 1 h in the previous study) using the same RNA construct. Although the “i+1” product diminished over time, the amount of “i+3” (P20) did not apparently decrease in the tested period, indicating that at least a portion of catalytic complexes terminated or became inactive at this stage (Figure 1D, lanes 83–94; Figure S1). As expected, both “i+1” and “i+3” products were not pronounced in the ATP comparison set (Figure 1D, lanes 63–74).

CellPress
OPEN ACCESS

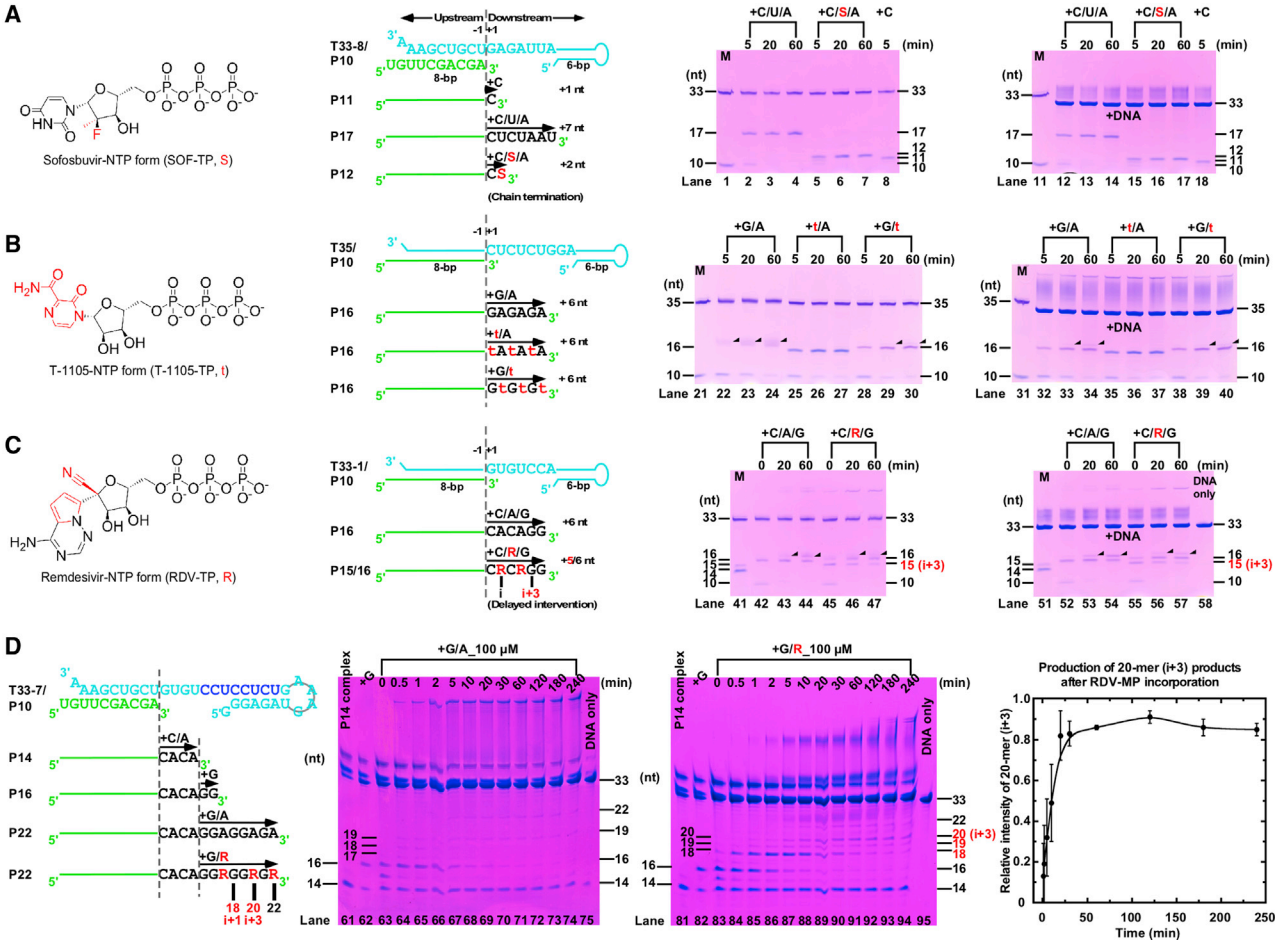

Figure 1. Three representative NA intervention types observed in SARS-CoV-2 RdRP

(A–C) Left: structural formulas of the NTP form of three representative NAs: (A) sofosbuvir (SOF or S), (B) T-1105 (t), and (C) remdesivir (RDV or R). Parts of each NA that differ from regular nucleotide are shown in red. Middle: RNA constructs used in primer-dependent polymerase assays and the expected product species obtained with different NTP combinations. Right: denaturing PAGE analysis of the RNA species in extension reactions. A DNA complementary to the template RNA was added to help resolve relatively long RNA products. Solid triangles indicate products derived from misincorporation. For positions "i" and "i+x," "i" corresponds to the position of the first incorporated RDV and "x" denotes x position following the first RDV incorporation.

(D) Left: the RNA construct used in time-course primer-dependent polymerase assays and the expected product species obtained with different NTP combinations following the assembly and chromatographic purification of a P14-containing catalytic complex. Middle: denaturing PAGE analysis of the RNA species in extension reactions with G/A or G/R combinations. Right: an analysis of the production of 20-mer (i+3) with G/R combination (also see Figure S1). The maximum intensity of the 20-mer band is set as 0.9. The average relative intensity values with standard deviations (error bars) obtained from three individual experiments were plotted against reaction time, with the trend indicated by a smooth curve based on the algorithm of Stineman.

M, RNA length markers.

A 3.0-Å cryo-EM structure of SARS-CoV-2 RdRP EC indicates critical interactions for complex stability

Because complex stability level is one of the important factors affecting the fate of product nucleic acid strand in polymerases, the delayed intervention is likely situation dependent and may be affected by multiple factors. To achieve a better understanding of RDV intervention on SARS-CoV-2 RdRP, we assembled a catalytic complex using a T56/P10×3 construct and compared it with a previously reported P14-containing complex derived from T33-1/P10 (Wang et al., 2020c) (Figure 2). By annealing the P10 RNA to a 56-mer template (T56), three P10 can form an array and result in a 28-bp duplexed region prior to catalysis (Figure 2B). Such long RNA duplexes, if present at upstream of the SARS-CoV-2 catalytic complex active site, were shown to interact with two nsp8 molecules, potentially providing extra stabilization of the complex (Chen et al., 2020; Hillen et al., 2020). Catalytic complexes were assembled by incubating the T33-1- and T56-derived RNA constructs with nsp12, nsp7, and nsp8 in the presence of CTP and ATP and then purified by anion exchange chromatography (Figures 2A and 2B). We first assessed complex reactivity at 4°C and 25°C and found that both complexes can rapidly incorporate 2 nt to form 16-mer (P16)-containing complexes (Figures 2A and 2B, lanes 2, 12, 22, and 32), except that a fraction of the T33-1-derived complex failed to react, possibly because of dissociation or inactivation (Figures 2A and 2B, lanes 2–8 and 12–18). Although the difference in

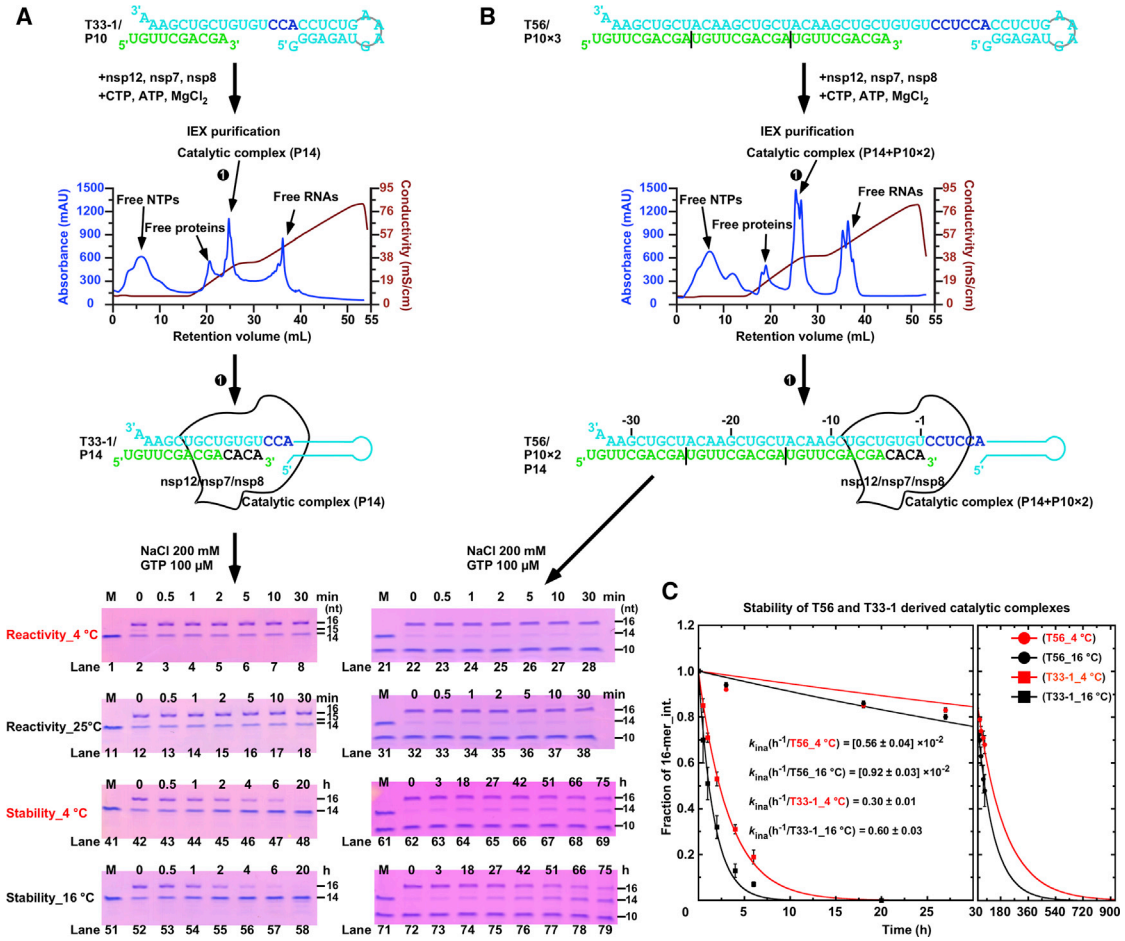

Figure 2. A comparison of reactivity and stability of T33- and T56-derived RdRP catalytic complexes

(A and B) Top: T33-1/P10- (A) and T56/P10×3-derived (B) P14-containing catalytic complexes assembly and purification. Bottom: denaturing PAGE analysis to assess the reactivity and stability of catalytic complexes by monitoring the extension of P14 to P16 upon GTP addition.

(C) The average fraction of P16 intensity values with standard deviations (error bars) obtained from four individual experiments were plotted against the incubation time prior to the addition of GTP, and the fitted inactivation rate constants (k_{ina}) were indicated (also see Figure S2).

reactivity of both complexes was not observed in the manual-mixing experimental settings, complex stability levels were indeed quite different (Figures 2A and 2B, compare lanes 41–58 with lanes 61–79; Figure S2). The T33-1-derived complex had estimated inactivation rate constants (k_{ina}) of about 0.3 and 0.6 h^{-1} (corresponding to half-life values of 2.6 and 1.2 h) at 4°C and 16°C, respectively. The T56-derived complex exhibited much higher stability with k_{ina} values about 0.006 and 0.009 h^{-1} (corresponding to half-life values of 115 and 77 h). The slow inactivation and high reactivity of the T56-derived complex indicate that SARS-CoV-2 RdRP can form a *bona fide* EC with a combination of upstream RNA-nsp8 interactions and several rounds of nucleotide incorporation.

Although SARS-CoV-2 RdRP-RNA complexes have been solved using RNA constructs with similar length as T56/P10×3, none of these structures were obtained after multiple nucleotide addition cycles (NACs) (Chen et al., 2020; Hillen et al., 2020; Yan et al., 2021), making it difficult to identify structural requirements for EC assembly. To structurally understand the gain in stability of the T56-derived P14-containing EC that was assembled after four NACs and to identify key interactions in EC assembly by comparison with previously reported CoV RdRP-RNA complexes, we solved a 3.0-Å resolution cryo-EM structure of this P14-containing EC in the presence of an incoming 3′-deoxy-GTP (3dGTP) (Figure 3A; Table S1; Figures S3 and S4). Due to relatively weak EM density, we did not model the 3dG nucleotide in this structure (Figure S4). The density of the template-product RNA gets weaker toward the upstream end, allowing the modeling of the double-stranded (ds) region up to position −21 (Figures 2B and 3A). Interactions between the N-terminal helices of the two nsp8 molecules and the upstream dsRNA were clearly observed, similar to those observed in long RNA-derived SARS-CoV-2 polymerase complex EM structures (Chen et al., 2020; Hillen et al., 2020; Yan et al., 2020, 2021), confirming their contribution to complex stability. This type of interaction may be unique for CoV or *Nidovirales* RdRPs because other viral RdRPs or RdRP complexes appear not to contain elements long enough to reach upstream dsRNA about 50 Å away from the right-hand shape

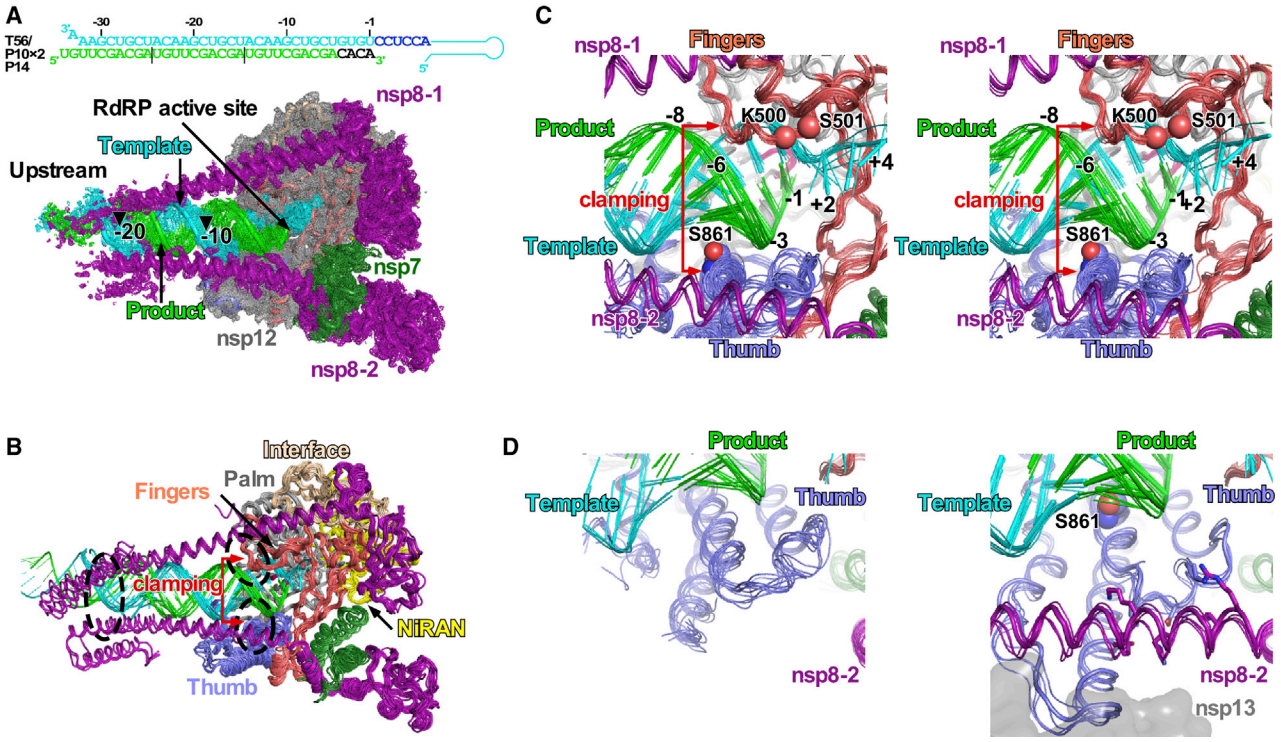

Figure 3. Critical interactions and conformational changes for SARS-CoV-2 RdRP elongation complex (EC) formation

(A) Cryo-EM density map (contoured at 3 σ) of the T56-derived P14-containing EC with the structure in cartoon representation overlaid. Coloring scheme: nsp12, gray; nsp7, dark green; nsp8, purple; RNA template, cyan; RNA product, green. Numbers and solid triangles indicated reference positions in the upstream RNA.

(B) A superimposition of CoV RdRP structures in cartoon representations. The coloring scheme is the same as in (A), except that nsp12 is subdivided and re-colored: palm, gray; fingers, light red; thumb, slate; NiRAN (nidovirus RdRP-associated nucleotidyltransferase), yellow; interface, wheat. The interactions between the two nsp8 molecules and the upstream dsRNA are indicated by a dashed oval. The dsRNA clamping interactions provided by a thumb domain helix and fingers domain motif G are indicated by two dashed ovals and the red arrows.

(C) A close-up view (as stereo-pair images) of the clamping interactions. The S861 and the α-carbon atoms of two critical motif G residues are shown as spheres. The T56-derived EC is shown by thick representations.

(D) The conformation of the thumb tip is dependent on the interaction between the thumb and nsp8-2. The thumb tip is disordered in the absence of thumb-nsp8-2 interactions (left) and consistently folded when interacting with nsp8-2 (right). Part of the fingers domain is not shown for clarity.

polymerase core. It is possible that the CoV RdRPs require extra processivity to complete the relatively long RNA genome and have evolved these auxiliary interactions.

By superimposing the T56-derived EC structure with representative CoV RdRP structures in the Protein Data Bank (PDB), we were able to extract other critical interactions and structural elements responsible for complex stability. Similar to other RdRPs, the template-product RNA within the polymerase core was clamped by RdRP motif G and a thumb helix (the S861-containing helix in SARS-CoV-2 nsp12) through contacts with major and minor grooves, respectively (Appleby et al., 2015; Gong et al., 2013; Gong and Peersen, 2010; Kouba et al., 2019) (Figures 3B and 3C). It turned out that the long loop at the thumb tip (nsp12 residues 844–855) connecting to this clamping helix exhibited two conformation populations (Figures 3C and 3D). One population was represented by the apo structures and the majority of short RNA-derived complex structures (Figure 3D, left). The other population included all long-RNA-derived complexes and those with nsp13 bound, with this loop flipped away from the RNA, and formed interactions with the long helix of nsp8-2 that bridges the polymerase core and the upstream RNA (Figure 3D, right). The establishment of these interactions also helps the folding of the neighboring thumb tip region (residues 896–913) that participates in nsp8-2 and nsp13 binding (Chen et al., 2020; Yan et al., 2020, 2021). Hence the cooperation of the RdRP-conserved clamping interactions and the CoV-characteristic upstream interactions are likely responsible for ideal processivity of the CoV catalytic complex, and the conformational switch of the thumb tip plays a critical role in establishment of the nsp8-mediated upstream interactions. It is also worth mentioning that nsp13 molecules are likely recruited to the replication/transcription complex (RTC) after EC formation, because both nsp13 molecules interact with the EC form of nsp8-1 and nsp8-2 (Chen et al., 2020; Yan et al., 2020, 2021).

RDV may induce temporal pausing only on SARS-CoV-2 RdRP EC

We next assessed RDV intervention in the T56-derived EC in a time-course format (Figure 4). When G, A, and UTP (G/A/U) were supplied to the purified P14-containing EC, the complex was expected to synthesize a 25-mer product (P25). The reaction temperature was set at 0°C to aid the observation of the time-dependent

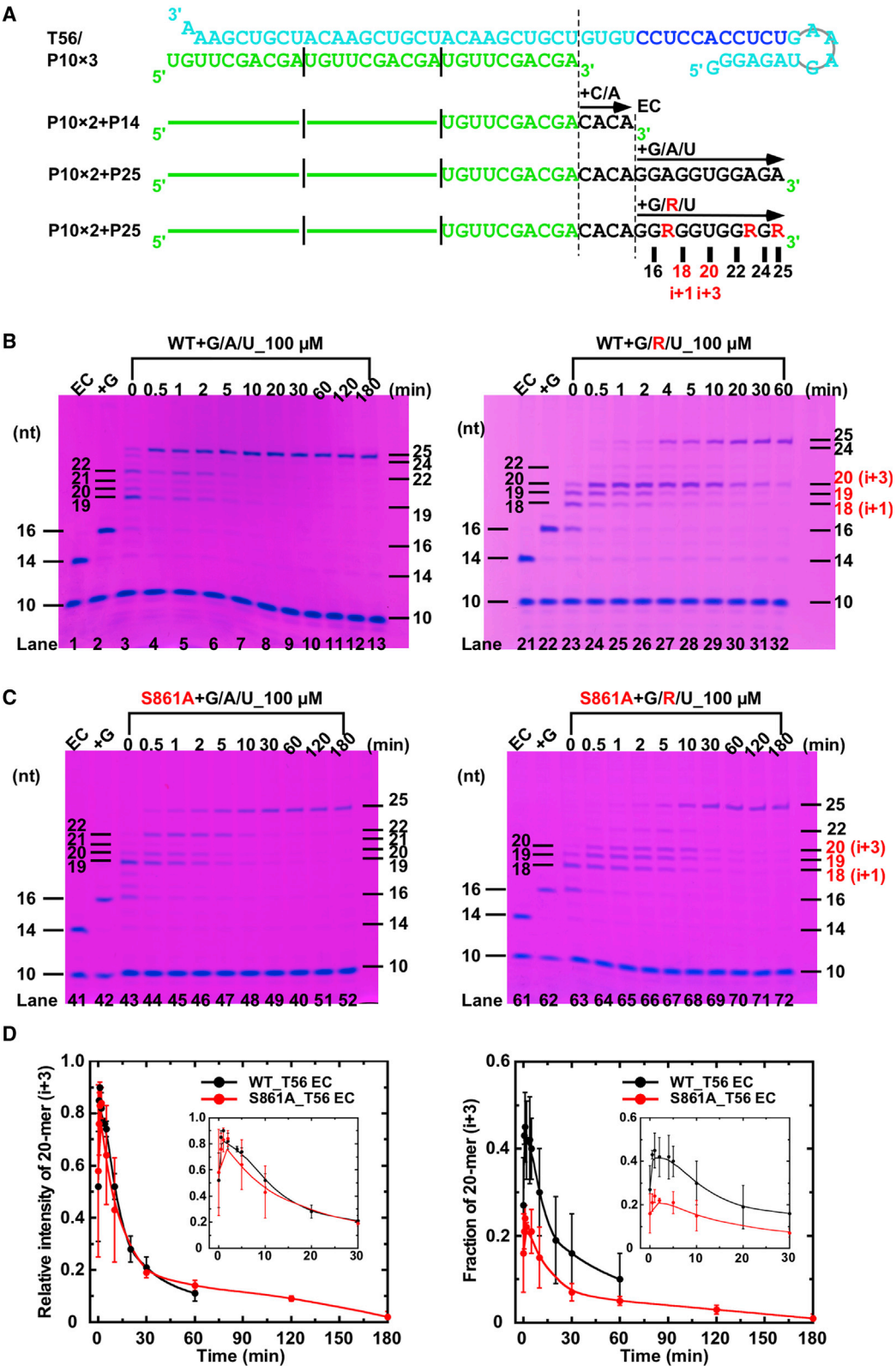

(legend on next page)

extension. At early time points (0–5 min), intermediate products of 19- to 22-mer were observed (Figure 4B, lanes 3–7). The majority of these products were readily extended over time, indicating an overall processive polymerization process (Figure 4B, lanes 8–13). When ATP was replaced by RDV-TP in the NTP mixture (G/R/U), "i+1" to "i+3" intermediate products (corresponding to 18- to 20-mer) were observed in early time points (0–2 min) (Figure 4B, lanes 23–26). The "i+1" and "i+2" products did not further accumulate and were mostly extended beyond the 2-min time point (Figure 4B, lanes 27–32). The 20-mer "i+3" product (P20), however, exhibited a "bell" shape distribution over time with a maximum level observed around 1–2 min (Figure 4B, lanes 23–32). This observation is different from that observed on the T33-7-derived complex under similar reaction conditions, where no obvious decrease of "i+3" amount was observed even after 4 h of reaction (Figure 1D, lanes 83–94 and right panel). When the reaction temperature was slightly increased (to 6°C), complete extension of the "i+3" product was observed within the same period (Figure S5). Hence RDV can induce an "i+3" pausing in a SARS-CoV-2 EC, and subsequent elongation is allowed for the entire RdRP population even under relatively low temperature. Also using gel-based approaches, similar readthroughs of RDV intervention were recently reported (Kokic et al., 2021; Tchesnokov et al., 2020).

Both structural analysis and enzymology data support the relationship between the "i+3" intervention and the SARS-CoV-2 RdRP thumb residue S861 (Gordon et al., 2020; Tchesnokov et al., 2020; Wang et al., 2020c). This serine residue poises near the product strand backbone at the −4 position. After the incorporation of the "i+3" nucleotide, the 1′-cyano group of the pre-incorporated RDV needs to translocate from position −3 to position −4 and likely interferes with the S861 side chain (Gordon et al., 2020). Indeed, the SARS-CoV-2 nsp12 S861A mutant reduced the fraction of "i+3" product on the T33-1 template (Wang et al., 2020c). Here we further assessed this effect of this mutation on the T56-derived EC (Figure 4C). For regular G/A/U addition, the S861A mutant behaves similarly to the wild-type (WT) enzyme, with slightly slower conversion of the intermediate products (Figures 4B and 4C, compare lanes 3–13 with 43–52). Not surprisingly, the time-dependent profile of "i+1" to "i+3" products in the G/R/U reaction was altered by the S861A mutation. The "i+3" product was no longer prominent among the intermediate products and the fraction of the "i+3" production decreased, if compared with SARS-CoV-2 nsp12 WT (compare Figures 4B and 4C, compare lanes 23–32 with 63–72; Figure 4D; Figure S6), and its accumulation and conversion process almost follow the trend of its precedent "i+2" product (Figure 4C, lanes 63–72). Collectively, these data further emphasize the relevance of S861 in "i+3"-related intervention.

RDV exhibits broad-spectrum intervention against other RNA virus polymerases

In order to understand the broad-spectrum intervention potential of RDV and its possible encounter of the clamping thumb helix in non-CoV systems, we tested RDV intervention in three other viral RdRPs: HCV NS5B, dengue virus serotype 2 (DENV2) NS5, and EV71 $3D^{pol}$. HCV and DENV2 both belong to the *Flaviviridae*, and their RdRPs are representatives of *de novo* polymerases. We used a previously established dinucleotide-driven assay to compare the ATP/UTP and RDV-TP/UTP incorporation of HCV and DENV2 RdRPs (Figure 5A). Although the HCV NS5B incorporated RDV as efficiently as ATP (Figure 5A, compare lanes 1–3 with 4–6), DENV2 NS5 exhibited clearly lower RDV incorporation efficiency (Figure 5A, compare lanes 11–13 with 14–16). Interestingly, no prominent delayed intervention induced by RDV was evident in these two RdRPs, although low-level accumulation of 5-mer (corresponding to "i+2") and 6-mer (corresponding to "i+3") was observed for HCV NS5B and DENV NS5, respectively. We then tested RDV intervention in the primer-dependent *Picornaviridae* EV71 RdRP that also contains a serine (S417) at the SARS-CoV-2 nsp12 S861 equivalent position using the T33-1/P10 construct (Figure 5B). In the presence of CTP and ATP (C/A), EV71 RdRP efficiently extended the P10 primer to P14 product within 30 min (Figure 5B, lanes 2–5). In the presence of CTP and RDV-TP (C/R), extension with similar efficiency was observed with more pronounced 15-mer product likely because of misincorporation (Figure 5B, compare lanes 2–5 with 6–9). With both NTP combinations, there were not many intermediate bands observed (Figure 5B, lanes 2–5 and 7–9), except that 11-mer and 13-mer bands were observed at the "0 min" time point for the G/R combination (Figure 5B, lane 6), suggesting that there was only minor intervention induced by RDV during the entire process. We then compared the extension profiles with C/A/G (GTP) and C/R/G combinations. Although P16 product formation was observed in both cases, only the latter resulted in continuous observation of the "i+3" 15-mer product over time (Figure 5B, lanes 16–19). These data together suggest that RDV can also induce delayed intervention on EV71 RdRP at the SARS-CoV-2 nsp12 S861-equivalent site. Next, we tested different incoming GTP concentrations (with respect to the "i+3" event) and compared the extension profiles of WT RdRP and three S417 mutants. For the WT enzyme, the 15-mer amount gradually decreased after the 1-min time point at 300 μM GTP concentration but persisted at high level in the same period at 20 μM GTP concentration, suggesting that the competition between extension and RDV-induced dissociation/inactivation determines the fate of "i+3" product (Figure 5C, compare lanes 5–8 with 15–18). For the S417T and S417A mutants, the fraction of 15-mer is generally lower than that of the WT (Figure 5C, compare lanes 4–18 with

Figure 4. RDV-induced temporal pausing at "i+3" was observed in T56-derived RdRP EC

(A) The expected product species obtained with different NTP combinations following the assembly and chromatographic purification of the P14-containing EC.
(B and C) Denaturing PAGE analysis of the RNA species in extension reactions with G/A/U (left) or G/R/U (right) combinations for ECs assembled using WT nsp12 and the S861A mutant.
(D) Time-dependent 20-mer (i+3) amount comparison with G/R/U combination in EC extension assay using WT nsp12 and S861A mutant (also see Figure S6). Left: comparison of the relative intensity with maximum intensity set to 0.9 for each construct. Right: comparison of the fraction of 20-mer intensity among all 15- to 25-mer species. Smooth curves are used to show corresponding trends based on the algorithm of Stineman. Each data point is the average value with standard deviation (error bars) derived from three individual experiments.

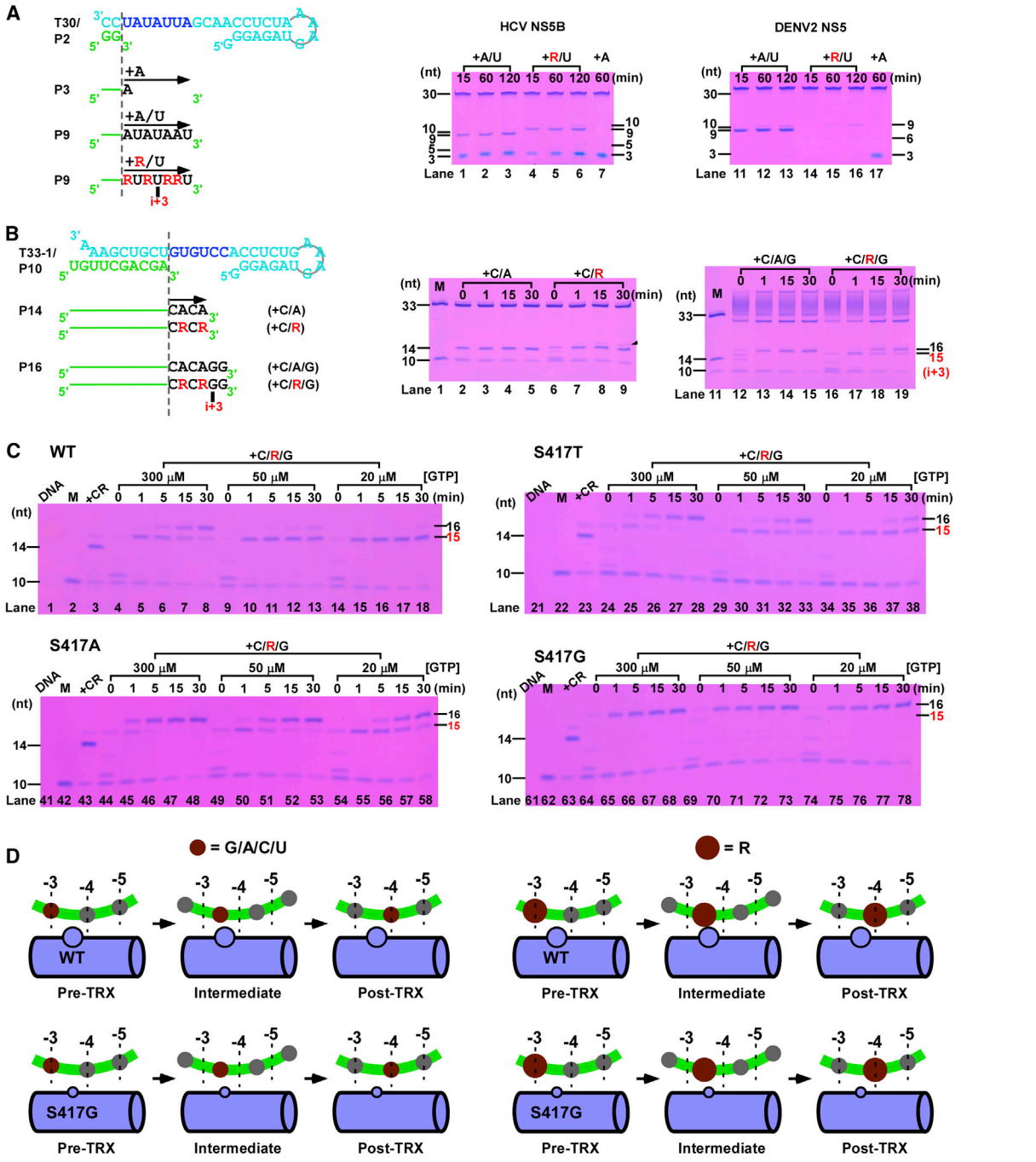

Figure 5. RDV-induced delayed intervention was also observed in EV71 RdRP

(A and B) Left: the T30/P2 (A) and T33/P10 (B) RNA constructs used in the dinucleotide-driven (A) or primer-dependent (B) polymerase assays for HCV/DENV2 (A) and EV71 (B) systems and the expected product species with different NTP combinations. Right: denaturing PAGE analysis of the RNA species.

(C) Denaturing PAGE analysis of the RNA species in extension reactions with C/R/G combination at three GTP concentrations for WT EV71 RdRP and three S417 mutants. A DNA complementary to the template RNA was added to help resolve relatively long RNA products.

(D) A schematic illustration of the relationship between residue 417 (black circle) and the product strand nucleotide (brown sphere) translocating from position −3 to position −4. Top left: regular NMP gets through S417 smoothly; bottom left: S417G may lose the role of "lubricating" translocation; top right: bulkier RDV clashes with S417 and causes intervention during translocation; bottom right: small side-chain S417G better accommodates RDV during translocation.

DNA, DNA sample only; TRX, translocation.

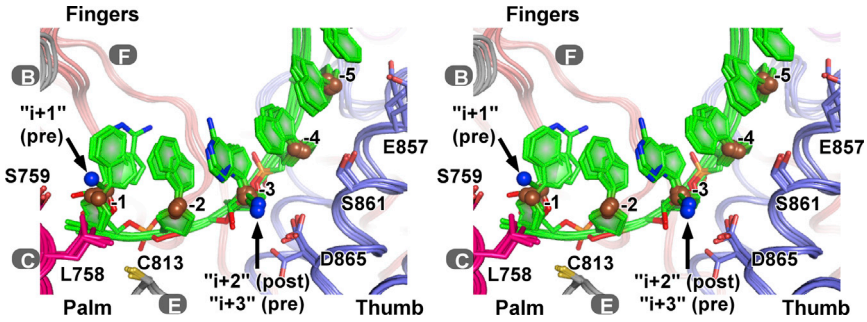

Figure 6. A comparison of RDV-containing SARS-CoV-2 RdRP-RNA structures

Three RDV-containing RdRP-RNA structures ("i+1," PDB: 7C2K; "i+2" post, PDB: 7B3B; "i+3" pre, PDB: 7B3C) are compared using the two RDV-free structures as references (PDB: 7DTE [EC in this work]; PDB: 7B3D) in the stereo-pair image format. The coloring scheme is the same as in Figure 3B. For clarity, the template RNA and part of RdRPs are not shown. The 1′-carbon atoms of the product RNA nucleotides (except for position +1) are shown as brown spheres and are used to indicate its moving track upon RdRP translocation events. The nitrogen atoms of the RDV 1′-cyano groups are shown as blue spheres. The product RNA positions are labeled. Capital letters with gray background indicate RdRP catalytic motifs. The RDV nucleotides are shown as sticks. For clarity, the +1 product (primer) nucleotide for the two pre-translocation complexes are not shown.

lanes 24–38 and 44–58), while the S417G mutant with the smallest side chain almost did not have 15-mer accumulated (Figure 5C, lanes 64–78). These observations demonstrate that EV71 RdRP S417 is involved in RDV-induced "i+3" intervention, and the steric encounter of the S417 side chain and RDV is responsible for this intervention. It is worth noting that the hydroxyl group of S417 side chain forms a hydrogen bond with the 2′-hydroxyl group of the −3 nt of the product RNA in previously reported EV71 RdRP translocation intermediate structures (PDB: 5F8N, 6LSE), but not in pre- or post-translocated RdRP ECs (Figure S7). Hence this residue or its equivalents in other RdRP systems may help the movement of the product RNA and contribute to the stability of RdRP catalytic complex during every translocation event (Video S1). Mutations of this residue to small side-chain residues may help accommodate the post-incorporation translocation of RDV through the −4 position but may lose the benefits in its facilitation in translocation for regular nucleotides (Figure 5D). In this regard, it will be difficult to predict whether RDV-resistant viruses containing mutation at this critical residue (e.g., SARS-CoV-2 nsp12 S861) can indeed emerge.

DISCUSSION

The unique delayed intervention mechanism of RDV makes it attractive for structural capturing of the direct encounter of the incorporated RDV and SARS-CoV-2 nsp12 S861 side chain. Using chemically synthesized RDV-containing RNA constructs in complex assembly, two RDV-containing SARS-CoV-2 RdRP-RNA complex structures were recently reported with RDV both poising at the −3 position of the primer strand (corresponding to the product strand in our work), one register downstream of the −4 position or the S861 site (Kokic et al., 2021). According to the "i+x" nomenclature and translocational state, these two structures represent a post-translocation "i+2" complex and a pre-translocation "i+3" complex. Together with the pre-translocation "i+1" complex structure we reported previously, these structures provide a general view of RDV movement track after its incorporation (Wang et al., 2020c) (Figure 6). However, the aforementioned direct encounter requires RDV to reach the −4 position. The EC assembly and structural analysis established in the current work provide the opportunity to capture a RDV-induced pausing EC with such an encounter, either using WT nsp12 or its S861 mutants. With a similar delayed intervention mechanism induced by RDV, the EV71 RdRP provides another suitable system to further dissect RDV intervention.

The delayed intervention of RDV attributed to its post-incorporation encounter with SARS-CoV-2 S861 side chain is a unique mechanism different from those represented by immediate-chain termination and error-prone synthesis caused by ambiguous base pairing. This intervention mechanism is directly related to the stepwise and periodic translocation of the product RNA strand in the continuous synthesis of RNA. By capturing three types of translocation intermediates, two in forward translocation and one in reverse translocation using the enterovirus 71 (EV71) RdRP system, we demonstrated that the product strand movement is not rate limiting in translocation (Shu and Gong, 2016; Wang et al., 2020b). By contrast, the interactions between the two motif G residues (T114-S115 in EV71 RdRP and equivalent to K500-S501 of SARS-CoV-2 nsp12) and the template strand backbone around the active site stringently control the movement of the template strand, resulting in the asymmetric nature in dsRNA movement during RdRP translocation (Wang et al., 2020b). The introduction of RDV into the product strand may change this situation by hindering product strand movement at a particular stage, for example, the translocation event corresponding to the movement of RDV from position −3 to position −4. This position-dependent intervention of product strand movement may also be applied to other viral RdRPs for RDV and other 1′-modified NAs. Here we compared the product strand backbone moving track of the four representative viral RdRPs, SARS-CoV-2 nsp12, EV71 $3D^{pol}$, HCV NS5B, and influenza A virus PB1, by investigating the interactions between the product strand backbone and the polymerase. Despite drastic differences in global architecture and primary structure of these polymerases or corresponding polymerase complexes (Appleby et al., 2015; Kouba et al., 2019; Shu and Gong, 2016; Wang et al., 2020c), the structural elements interacting with the product strand backbone are highly analogous (Figure 7). RdRP motif C, motif E, and the aforementioned clamping thumb helix relay in the moving track, interacting with the +1/−1, −2, and −3 to −5 positions of the backbone, respectively. Each of these three structural elements contain side chains within 7 Å to the 1′-carbon of the corresponding product nucleotide. Among these residues, equivalents to SARS-CoV-2 nsp12 S861 are all spatially close to the −4 nt, with the distance between the 1′-carbon and the β-carbon (serine)/α-carbon (glycine) shorter than 5 Å. Hence 1′-modified NAs, depending on the substitution group,

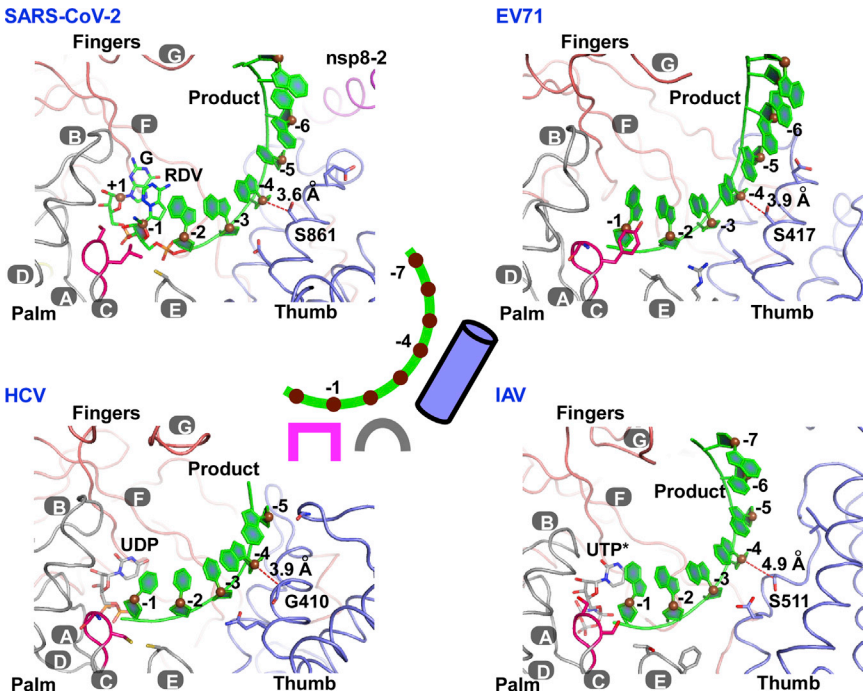

Figure 7. A structural comparison of RNA product moving track in four representative viral RdRPs

Top left: SARS-CoV-2 nsp12 (PDB: 7C2K); top right: EV71 3D^{pol} (PDB: 5F8G); bottom left: HCV NS5B (PDB: 4WTA); bottom right: influenza A virus PB1 (PDB: 6T0V). The coloring scheme is the same as in Figure 3B. For clarity, the template RNA and part of RdRPs are not shown. The 1′-carbon atoms of the product RNA nucleotides (except for position +1) are shown as brown spheres and are used to indicate its moving track upon RdRP translocation events. The product RNA positions are labeled. Capital letters with gray background indicate RdRP catalytic motifs. The +1 and −1 product nucleotides (G and R) of the SARS-CoV-2 structure, the UDP in the HCV structure, and the UTP analog (*UTP) in the IAV structure are shown as sticks. Glycines and side chains of non-glycine residues within 8 Å of each product nucleotide 1′-carbon atom are shown as sticks. Center: a sketch of spatial relationship between the product RNA backbone and three structurally conserved RdRP elements.

may cause intervention at any position between −1 and −5 during its post-incorporation translocation events, and the intervention at the −4 position (corresponding to the "i+3" event) may have higher possibilities.

By combining enzymology and structural approaches, we have obtained improved understandings of the delayed intervention of RDV, an NA with characteristic modification at the ribose 1′-position. RDV-TP can be efficiently incorporated, allow subsequent catalysis, and under certain circumstances allow processive synthesis through bypassing the corresponding "i+3"-related SARS-CoV-2 nsp12 S861 site or EV71 3D^{pol} S417 site. Hence RDV might indeed become part of the RNA template, as has been tested in a recent enzymology study (Tchesnokov et al., 2020), or affect post-transcription events. It is conceivable for RDV to induce intervention when passing through the active site as a templating nucleotide, because the template backbone around here is sterically controlled by the motif G "hurdle residues" proposed in our previous EV71 work (Wang et al., 2020b). Moreover, the capability to readthrough the intervention site may allow RDV to evade proofreading processes essential for CoVs, at least at the delayed intervention stage. It is therefore quite interesting to investigate the incorporation frequency and nucleotide sequence context of RDV at the viral genome level, not only for SARS-CoV-2 but also for RNA viruses in general.

Limitations of the study

The current study reveals that RDV can overcome the S861 roadblock in a SARS-CoV-2 RdRP EC, while a similar mechanism is found in the EV71 system. However, the direct encounter of the incorporated RDV and the roadblock residue has not been captured by structural biology approaches in either system. Besides, the current study assesses only RdRP systems from several positive-strand RNA viruses regarding the RDV catalytic efficiency and delayed intervention mechanisms. Assessment in more representative viral RdRPs is necessary to achieve a comprehensive understanding of RdRP intervention by RDV.

STAR★METHODS

Detailed methods are provided in the online version of this paper and include the following:

- KEY RESOURCES TABLE
- RESOURCE AVAILABILITY
  - Lead contact
  - Materials availability
  - Data and code availability
- EXPERIMENTAL MODEL AND SUBJECT DETAILS
- METHOD DETAILS
  - Production of replication proteins from SARS-CoV-2 and other RNA viruses
  - RNA preparation and RdRP catalytic complex assembly
  - Cryo-EM Grid Preparation and Data Collection
  - Cryo-EM Image Processing and structure determination
  - *In vitro* primer-dependent RdRP assays for SARS-CoV-2 and other RNA viruses
- QUANTIFICATION AND STATISTICAL ANALYSIS

SUPPLEMENTAL INFORMATION

Supplemental information can be found online at https://doi.org/10.1016/j.celrep.2021.109882.

ACKNOWLEDGMENTS

We thank Dr. Olve Peersen for providing the HCV polymerase production plasmid; Dr. Bo Zhang for providing the cloning materials for the EV71 and DENV2 polymerase genes; Dr. Irina Artsimovitch for helpful discussion; and the Bio-Electron Microscopy Facility, ShanghaiTech University, and the Core Facility and Technical Support, Wuhan Institute of Virology for access to instruments. This work was supported by the National Key Research and Development Program of China (2018YFA0507200 to P.G.; 2017YFC0840300 and 2020YFA0707500 to Z.R.), the National Natural Science Foundation of China (32041007 and 32070185 to P.G.; 81520108019 and 813300237 to Z.R.; 32000136 to J.W.), the Young Talent Program of Health Commission of Hubei Province, China (WJ2021Q055 to J.W.), the Chinese Academy of Sciences Funds: the Advanced Customer Cultivation Project of Wuhan National Biosafety Laboratory (2021ACCP-MS10 to P.G.), and the Special Research Assistant Program (2021000041 to J.W.).

AUTHOR CONTRIBUTIONS

P.G., Z.R., and Q.W. conceived and coordinated the research; J.W., H.W., Q.L., X.F., and Y.Z. performed the CoV protein purification; J.W., Q.L., and X.F. performed the RNA template preparation; J.W., H.W., Q.L., and X.F. performed the EC assembly and purification; H.W. and Y.G. collected and processed the cryo-EM data; Q.W. and Y.G. built and refined the structural model; J.W., Q.L., X.F., and Y.Z. carried out the CoV enzymology experiments; R.L. and M.W. performed EV71 RdRP mutant plasmid construction, protein preparation, and enzymology experiments; P.G., Q.W., J.W., and Z.R. wrote the manuscript; and all authors discussed and approved the manuscript content.

DECLARATION OF INTERESTS

The authors declare no competing interests.

Received: March 8, 2021
Revised: July 5, 2021
Accepted: October 4, 2021
Published: October 8, 2021

REFERENCES

Adams, P.D., Baker, D., Brunger, A.T., Das, R., DiMaio, F., Read, R.J., Richardson, D.C., Richardson, J.S., and Terwilliger, T.C. (2013). Advances, interactions, and future developments in the CNS, Phenix, and Rosetta structural biology software systems. Annu. Rev. Biophys. *42*, 265–287.

Afonine, P.V., Grosse-Kunstleve, R.W., Echols, N., Headd, J.J., Moriarty, N.W., Mustyakimov, M., Terwilliger, T.C., Urzhumtsev, A., Zwart, P.H., and Adams, P.D. (2012). Towards automated crystallographic structure refinement with phenix.refine. Acta Crystallogr. D Biol. Crystallogr. *68*, 352–367.

Appleby, T.C., Perry, J.K., Murakami, E., Barauskas, O., Feng, J., Cho, A., Fox, D., 3rd, Wetmore, D.R., McGrath, M.E., Ray, A.S., et al. (2015). Viral replication. Structural basis for RNA replication by the hepatitis C virus polymerase. Science *347*, 771–775.

Batey, R.T., and Kieft, J.S. (2007). Improved native affinity purification of RNA. RNA *13*, 1384–1389.

Beigel, J.H., Tomashek, K.M., Dodd, L.E., Mehta, A.K., Zingman, B.S., Kalil, A.C., Hohmann, E., Chu, H.Y., Luetkemeyer, A., Kline, S., et al.; ACTT-1 Study Group Members (2020). Remdesivir for the Treatment of Covid-19 - Final Report. N. Engl. J. Med. *383*, 1813–1826.

Cardone, G., Heymann, J.B., and Steven, A.C. (2013). One number does not fit all: mapping local variations in resolution in cryo-EM reconstructions. J. Struct. Biol. *184*, 226–236.

Chen, J., Malone, B., Llewellyn, E., Grasso, M., Shelton, P.M.M., Olinares, P.D.B., Maruthi, K., Eng, E.T., Vatandaslar, H., Chait, B.T., et al. (2020). Structural Basis for Helicase-Polymerase Coupling in the SARS-CoV-2 Replication-Transcription Complex. Cell *182*, 1560–1573.e13.

Crotty, S., Cameron, C.E., and Andino, R. (2001). RNA virus error catastrophe: direct molecular test by using ribavirin. Proc. Natl. Acad. Sci. USA *98*, 6895–6900.

De Clercq, E., and Li, G. (2016). Approved Antiviral Drugs over the Past 50 Years. Clin. Microbiol. Rev. *29*, 695–747.

Du, Y.X., and Chen, X.P. (2020). Response to "Dose Rationale for Favipiravir Use in Patients Infected With SARS-CoV-2". Clin. Pharmacol. Ther. *108*, 190.

Elion, G.B., Furman, P.A., Fyfe, J.A., de Miranda, P., Beauchamp, L., and Schaeffer, H.J. (1977). Selectivity of action of an antiherpetic agent, 9-(2-hydroxyethoxymethyl) guanine. Proc. Natl. Acad. Sci. USA *74*, 5716–5720.

Emsley, P., Lohkamp, B., Scott, W.G., and Cowtan, K. (2010). Features and development of Coot. Acta Crystallogr. D Biol. Crystallogr. *66*, 486–501.

Furuta, Y., Gowen, B.B., Takahashi, K., Shiraki, K., Smee, D.F., and Barnard, D.L. (2013). Favipiravir (T-705), a novel viral RNA polymerase inhibitor. Antiviral Res. *100*, 446–454.

Gane, E.J., Stedman, C.A., Hyland, R.H., Ding, X., Svarovskaia, E., Symonds, W.T., Hindes, R.G., and Berrey, M.M. (2013). Nucleotide polymerase inhibitor sofosbuvir plus ribavirin for hepatitis C. N. Engl. J. Med. *368*, 34–44.

Gane, E.J., Stedman, C.A., Hyland, R.H., Ding, X., Svarovskaia, E., Subramanian, G.M., Symonds, W.T., McHutchison, J.G., and Pang, P.S. (2014). Efficacy of nucleotide polymerase inhibitor sofosbuvir plus the NS5A inhibitor ledipasvir or the NS5B non-nucleoside inhibitor GS-9669 against HCV genotype 1 infection. Gastroenterology *146*, 736–743.e1.

Goddard, T.D., Huang, C.C., Meng, E.C., Pettersen, E.F., Couch, G.S., Morris, J.H., and Ferrin, T.E. (2018). UCSF ChimeraX: Meeting modern challenges in visualization and analysis. Protein Sci. *27*, 14–25.

Gohara, D.W., Ha, C.S., Kumar, S., Ghosh, B., Arnold, J.J., Wisniewski, T.J., and Cameron, C.E. (1999). Production of "authentic" poliovirus RNA-dependent RNA polymerase (3D(pol)) by ubiquitin-protease-mediated cleavage in Escherichia coli. Protein Expr. Purif. *17*, 128–138.

Goldman, J.D., Lye, D.C.B., Hui, D.S., Marks, K.M., Bruno, R., Montejano, R., Spinner, C.D., Galli, M., Ahn, M.Y., Nahass, R.G., et al.; GS-US-540-5773 Investigators (2020). Remdesivir for 5 or 10 Days in Patients with Severe Covid-19. N. Engl. J. Med. *383*, 1827–1837.

Gong, P., and Peersen, O.B. (2010). Structural basis for active site closure by the poliovirus RNA-dependent RNA polymerase. Proc. Natl. Acad. Sci. USA *107*, 22505–22510.

Gong, P., Kortus, M.G., Nix, J.C., Davis, R.E., and Peersen, O.B. (2013). Structures of coxsackievirus, rhinovirus, and poliovirus polymerase elongation complexes solved by engineering RNA mediated crystal contacts. PLoS ONE *8*, e60272.

Gordon, C.J., Tchesnokov, E.P., Woolner, E., Perry, J.K., Feng, J.Y., Porter, D.P., and Götte, M. (2020). Remdesivir is a direct-acting antiviral that inhibits RNA-dependent RNA polymerase from severe acute respiratory syndrome coronavirus 2 with high potency. J. Biol. Chem. *295*, 6785–6797.

Hakimelahi, G.H., Ly, T.W., Moosavi-Movahedi, A.A., Jain, M.L., Zakerinia, M., Davari, H., Mei, H.C., Sambaiah, T., Moshfegh, A.A., and Hakimelahi, S. (2001). Design, synthesis, and biological evaluation of novel nucleoside and nucleotide analogues as agents against DNA viruses and/or retroviruses. J. Med. Chem. *44*, 3710–3720.

Hillen, H.S., Kokic, G., Farnung, L., Dienemann, C., Tegunov, D., and Cramer, P. (2020). Structure of replicating SARS-CoV-2 polymerase. Nature *584*, 154–156.

Jacobs, M., Rodger, A., Bell, D.J., Bhagani, S., Cropley, I., Filipe, A., Gifford, R.J., Hopkins, S., Hughes, J., Jabeen, F., et al. (2016). Late Ebola virus relapse causing meningoencephalitis: a case report. Lancet *388*, 498–503.

Jin, Z., Smith, L.K., Rajwanshi, V.K., Kim, B., and Deval, J. (2013). The ambiguous base-pairing and high substrate efficiency of T-705 (Favipiravir) Ribofuranosyl 5′-triphosphate towards influenza A virus polymerase. PLoS ONE *8*, e68347.

Jin, Z., Tucker, K., Lin, X., Kao, C.C., Shaw, K., Tan, H., Symons, J., Behera, I., Rajwanshi, V.K., Dyatkina, N., et al. (2015). Biochemical Evaluation of the Inhibition Properties of Favipiravir and 2′-C-Methyl-Cytidine Triphosphates

against Human and Mouse Norovirus RNA Polymerases. Antimicrob. Agents Chemother. *59*, 7504–7516.

Jordheim, L.P., Durantel, D., Zoulim, F., and Dumontet, C. (2013). Advances in the development of nucleoside and nucleotide analogues for cancer and viral diseases. Nat. Rev. Drug Discov. *12*, 447–464.

Kokic, G., Hillen, H.S., Tegunov, D., Dienemann, C., Seitz, F., Schmitzova, J., Farnung, L., Siewert, A., Höbartner, C., and Cramer, P. (2021). Mechanism of SARS-CoV-2 polymerase stalling by remdesivir. Nat. Commun. *12*, 279.

Kouba, T., Drncová, P., and Cusack, S. (2019). Structural snapshots of actively transcribing influenza polymerase. Nat. Struct. Mol. Biol. *26*, 460–470.

Lu, G., and Gong, P. (2013). Crystal Structure of the full-length Japanese encephalitis virus NS5 reveals a conserved methyltransferase-polymerase interface. PLoS Pathog. *9*, e1003549.

Lu, G., Zhang, X., Zheng, W., Sun, J., Hua, L., Xu, L., Chu, X.J., Ding, S., and Xiong, W. (2020). Development of a Simple *In Vitro* Assay To Identify and Evaluate Nucleotide Analogs against SARS-CoV-2 RNA-Dependent RNA Polymerase. Antimicrob. Agents Chemother. *65*, e01508-20.

Mastronarde, D.N. (2005). Automated electron microscope tomography using robust prediction of specimen movements. J. Struct. Biol. *152*, 36–51.

Papworth, C., Bauer, J.C., and Braman, J.C. (1996). Site-directed mutagenesis in one day with >80% efficiency. Strategies *9*, 3–4.

Pettersen, E.F., Goddard, T.D., Huang, C.C., Couch, G.S., Greenblatt, D.M., Meng, E.C., and Ferrin, T.E. (2004). UCSF Chimera—a visualization system for exploratory research and analysis. J. Comput. Chem. *25*, 1605–1612.

Pfeiffer, J.K., and Kirkegaard, K. (2003). A single mutation in poliovirus RNA-dependent RNA polymerase confers resistance to mutagenic nucleotide analogs via increased fidelity. Proc. Natl. Acad. Sci. USA *100*, 7289–7294.

Potisopon, S., Ferron, F., Fattorini, V., Selisko, B., and Canard, B. (2017). Substrate selectivity of Dengue and Zika virus NS5 polymerase towards 2′-modified nucleotide analogues. Antiviral Res. *140*, 25–36.

Punjani, A., Rubinstein, J.L., Fleet, D.J., and Brubaker, M.A. (2017). cryoSPARC: algorithms for rapid unsupervised cryo-EM structure determination. Nat. Methods *14*, 290–296.

Rosenthal, P.B., and Henderson, R. (2003). Optimal determination of particle orientation, absolute hand, and contrast loss in single-particle electron cryomicroscopy. J. Mol. Biol. *333*, 721–745.

Shi, W., Ye, H.Q., Deng, C.L., Li, R., Zhang, B., and Gong, P. (2020). A nucleobase-binding pocket in a viral RNA-dependent RNA polymerase contributes to elongation complex stability. Nucleic Acids Res. *48*, 1392–1405.

Shu, B., and Gong, P. (2016). Structural basis of viral RNA-dependent RNA polymerase catalysis and translocation. Proc. Natl. Acad. Sci. USA *113*, E4005–E4014.

Tan, Y.Z., Baldwin, P.R., Davis, J.H., Williamson, J.R., Potter, C.S., Carragher, B., and Lyumkis, D. (2017). Addressing preferred specimen orientation in single-particle cryo-EM through tilting. Nat. Methods *14*, 793–796.

Tchesnokov, E.P., Obikhod, A., Massud, I., Lisco, A., Vanpouille, C., Brichacek, B., Balzarini, J., McGuigan, C., Derudas, M., Margolis, L., et al. (2009). Mechanisms associated with HIV-1 resistance to acyclovir by the V75I mutation in reverse transcriptase. J. Biol. Chem. *284*, 21496–21504.

Tchesnokov, E.P., Feng, J.Y., Porter, D.P., and Götte, M. (2019). Mechanism of Inhibition of Ebola Virus RNA-Dependent RNA Polymerase by Remdesivir. Viruses *11*, 326.

Tchesnokov, E.P., Gordon, C.J., Woolner, E., Kocinkova, D., Perry, J.K., Feng, J.Y., Porter, D.P., and Götte, M. (2020). Template-dependent inhibition of coronavirus RNA-dependent RNA polymerase by remdesivir reveals a second mechanism of action. J. Biol. Chem. *295*, 16156–16165.

Theobald, D.L., and Wuttke, D.S. (2006). THESEUS: maximum likelihood superpositioning and analysis of macromolecular structures. Bioinformatics *22*, 2171–2172.

Wang, M., Cao, R., Zhang, L., Yang, X., Liu, J., Xu, M., Shi, Z., Hu, Z., Zhong, W., and Xiao, G. (2020a). Remdesivir and chloroquine effectively inhibit the recently emerged novel coronavirus (2019-nCoV) in vitro. Cell Res. *30*, 269–271.

Wang, M., Li, R., Shu, B., Jing, X., Ye, H.Q., and Gong, P. (2020b). Stringent control of the RNA-dependent RNA polymerase translocation revealed by multiple intermediate structures. Nat. Commun. *11*, 2605.

Wang, Q., Wu, J., Wang, H., Gao, Y., Liu, Q., Mu, A., Ji, W., Yan, L., Zhu, Y., Zhu, C., et al. (2020c). Structural Basis for RNA Replication by the SARS-CoV-2 Polymerase. Cell *182*, 417–428.e13.

Wolf, Y.I., Kazlauskas, D., Iranzo, J., Lucía-Sanz, A., Kuhn, J.H., Krupovic, M., Dolja, V.V., and Koonin, E.V. (2018). Origins and Evolution of the Global RNA Virome. MBio *9*, e02329-18.

Wu, J., Ye, H.Q., Zhang, Q.Y., Lu, G., Zhang, B., and Gong, P. (2020). A conformation-based intra-molecular initiation factor identified in the flavivirus RNA-dependent RNA polymerase. PLoS Pathog. *16*, e1008484.

Xu, H.T., Colby-Germinario, S.P., Hassounah, S.A., Fogarty, C., Osman, N., Palanisamy, N., Han, Y., Oliveira, M., Quan, Y., and Wainberg, M.A. (2017). Evaluation of Sofosbuvir (β-D-2′-deoxy-2′-α-fluoro-2′-β-C-methyluridine) as an inhibitor of Dengue virus replication. Sci. Rep. *7*, 6345.

Yan, L., Zhang, Y., Ge, J., Zheng, L., Gao, Y., Wang, T., Jia, Z., Wang, H., Huang, Y., Li, M., et al. (2020). Architecture of a SARS-CoV-2 mini replication and transcription complex. Nat. Commun. *11*, 5874.

Yan, L., Ge, J., Zheng, L., Zhang, Y., Gao, Y., Wang, T., Huang, Y., Yang, Y., Gao, S., Li, M., et al. (2021). Cryo-EM Structure of an Extended SARS-CoV-2 Replication and Transcription Complex Reveals an Intermediate State in Cap Synthesis. Cell *184*, 184–193.e10.

Zamyatkin, D.F., Parra, F., Alonso, J.M., Harki, D.A., Peterson, B.R., Grochulski, P., and Ng, K.K. (2008). Structural insights into mechanisms of catalysis and inhibition in Norwalk virus polymerase. J. Biol. Chem. *283*, 7705–7712.

Zheng, S.Q., Palovcak, E., Armache, J.P., Verba, K.A., Cheng, Y., and Agard, D.A. (2017). MotionCor2: anisotropic correction of beam-induced motion for improved cryo-electron microscopy. Nat. Methods *14*, 331–332.

Zivanov, J., Nakane, T., Forsberg, B.O., Kimanius, D., Hagen, W.J., Lindahl, E., and Scheres, S.H. (2018). New tools for automated high-resolution cryo-EM structure determination in RELION-3. eLife *7*, e42166.

STAR★METHODS

KEY RESOURCES TABLE

REAGENT or RESOURCE	SOURCE	IDENTIFIER
Bacterial and virus strains		
E.coli BL21(DE3)	Beijing ComWin Biotech	Cat# CW0809S
E.coli Rosetta(DE3)	Beijing ComWin Biotech	Cat# CW0811S
Chemicals, peptides, and recombinant proteins		
ATP	Sigma	Cat# A2383
GTP	Sigma	Cat# G8877
CTP	Sigma	Cat# C1506
UTP	Sigma	Cat# U6750
n-dodecyl-β-D-maltoside (DDM)	Anatrace	Cat# D310
Spermidine trihydrochloride	Sigma	Cat# S-2501
D-Gluocoseamine-6-phosphate	Sigma	Cat# G-5509
Acrylamide	Sangon Biotech	Cat# 79-06-1
DEPC-treated Water	ThermoFisher Scientific	Cat# 4387937
Boric acid	Sinopharm Chemical Reagent	Cat# 10004818
Tris(2-chloroethyl) Phosphate (TCEP)	Sigma	Cat# 115-96-8
Dithiothreitol (DTT)	Sinopharm Chemical Reagent	Cat# 3483-12-3
Magnesium chloride hexahydrate	Sigma	Cat# 7791-18-6
RDV-TP (2-C-(4-Aminopyrrolo[2,1-f][1,2,4] triazin-7-yl)-2,5-anhydro-D-altrononitrile triphosphate)	SeNtInall BioTechnologies	N/A
SOF-TP (2′-F-2′-C-Methyluridine-5′-TP)	SeNtInall BioTechnologies	N/A
T-1105-TP (4-((2R, 3S, 4R, 5R)-3,4-dihydroxy-5-(hydroxymethyl) tetrahydrofuran-2-yl)-3-oxo-3,4-dihydropyrazine-2-carboxamide triphosphate)	SeNtInall BioTechnologies	N/A
Deposited data		
Nsp12-nsp7-nsp8-RNA elongation complex EM map	This paper	EMDB: EMD-30852
Nsp12-nsp7-nsp8-RNA elongation complex structure	This paper	PDB: 7DTE
Nsp12-nsp7-nsp8-RNA complex structure	Wang et al., 2020a	PDB: 7C2K
Nsp12-nsp7-nsp8-RNA complex structure	Hillen et al., 2020	PDB: 6YYT
EV71 RdRP elongation complex in pre-translocation state	Shu and Gong, 2016	PDB: 5F8M
EV71 RdRP elongation complex translocation intermediate I	Shu and Gong, 2016	PDB: 5F8N
EV71 RdRP elongation complex translocation intermediate II	Wang et al., 2020b	PDB: 6LSH
EV71 RdRP elongation complex in post-translocation state	Shu and Gong, 2016	PDB: 5F8L
Oligonucleotides		
T33-1: GGGAGAUGAAAGUCUCCAC CUGUGUCGUCGAAA	This paper	N/A
T33-7: GGGAGAUGAAAGUCUCCU CCUGUGUCGUCGAAA	This paper	N/A

(*Continued on next page*)

Continued

REAGENT or RESOURCE	SOURCE	IDENTIFIER
T33-8: GGGAGAUGAAAGUCUCCA UUAGAGUCGUCGAAA	This paper	N/A
T35: GGGAGAUGAAAGUCUCCA GGUCUCUCUCGUCGAAA	This paper	N/A
T56: GGGAGAUGAAAGUCUCC ACCUCCUGUGUCGUCGAACA UCGUCGAACAUCGUCGAAA	This paper	N/A
P10: UGUUCGACGA	Integrated DNA Technologies (IDT)	N/A
Recombinant DNA		
pET22b-SARS-CoV-2-nsp12	Zhihe Rao and Quan Wang laboratories, ShanghaiTech University	N/A
pET28a-SARS-CoV-2-nsp7	Zhihe Rao and Quan Wang laboratories, ShanghaiTech University	N/A
pET28a-SARS-CoV-2-nsp8	Zhihe Rao and Quan Wang laboratories, ShanghaiTech University	N/A
pET22b-SARS-CoV-2-nsp12 S861A	This paper	N/A
pET26b-Ub-EV71 $3D^{pol}$	This paper	N/A
pET26b-DENV2-NS5	This paper	N/A
pET26b-HCV-NS5B	This paper	N/A
pRAV23	Jeffrey Kieft laboratory, University of Colorado School of Medicine	N/A
Software and algorithms		
SerialEM	Mastronarde, 2005	https://bio3d.colorado.edu/SerialEM/
MotionCor2	Zheng et al., 2017	https://emcore.ucsf.edu/ucsf-software
Gautomatch	Jack (Kai) Zhang	https://www2.mrc-lmb.cam.ac.uk/research/locally-developed-software/zhang-software/
ImageJ	National Institute of Health	https://imagej.nih.gov/ij/
RELION 3.03	Zivanov et al., 2018	https://www3.mrc-lmb.cam.ac.uk/relion/index.php/Main_Page
cryoSPARC	Punjani et al., 2017	https://cryosparc.com/
UCSF Chimera	Pettersen et al., 2004	https://www.cgl.ucsf.edu/chimera/
COOT	Emsley et al., 2010	https://www2.mrc-lmb.cam.ac.uk/personal/pemsley/coot/
PHENIX	Afonine et al., 2012	https://phenix-online.org/
PyMOL	Schrodinger	https://pymol.org/2/
UCSF ChimeraX	Goddard et al., 2018	https://www.cgl.ucsf.edu/chimerax/
KaleidaGraph	Synergy Software	https://www.synergy.com/
Other		
Quantifoil R0.6/1.0 200 mesh Cu holey carbon grids	Electron Microscopy Sciences	Cat# Q250CR-06

RESOURCE AVAILABILITY

Lead contact

Further information and requests for resources and reagents should be directed to and will be fulfilled by the Lead Contact, Peng Gong (gongpeng@wh.iov.cn).

Materials availability

All unique/stable reagents generated in this study are available from the Lead Contact without restriction.

Data and code availability

The cryo-EM maps and atomic coordinates for the reported structure have been deposited at the Protein Data Bank (PDB) and the Electron Microscopy Data Bank (EMDB) under accession codes 7DTE and EMD-30852, respectively.

This paper does not report original code.

Any additional information required to reanalyze the data reported in this paper is available from the lead contact upon request.

EXPERIMENTAL MODEL AND SUBJECT DETAILS

Proteins were obtained through recombinant expression in *E. coli* BL21(DE3) or *E. coli* Rosetta (DE3) strain.

METHOD DETAILS

Production of replication proteins from SARS-CoV-2 and other RNA viruses

The pET22b-based SARS-CoV-2 (GenBank: MN908947) nsp12 (WT and S861A mutant) production plasmids and pET28a-based nsp7/nsp8 production plasmids were transformed into *E. coli* BL21(DE3) to produce nsp12 with a C-terminal deca-histidine tag and nsp7 and nsp8 with an N-terminal hexa-histidine tag and a rhinovirus 3C protease cleavage sequence (LEVLFQGP)-based linker (Wang et al., 2020c). Cells were grown in LB medium containing 100 μg/ml ampicillin (AMP100) for nsp12 or 50 μg/ml kanamycin (KAN50) for nsp7 and nsp8 at 30°C overnight until the optical density at 600 nm (OD_{600}) was 1.0. The overnight culture was transferred to 1 l LB medium at a 1:50 (v/v) ratio. Cells were cultured at 37°C at 220 rpm to reach an OD_{600} of 1.0 and then cooled to 16°C. Isopropyl-β-D-thiogalactopyranoside (IPTG) was added to a final concentration of 0.5 mM, and the cells were grown for an additional 16 h at 16°C before harvesting.

The harvested cell pellets were resuspended in a lysis buffer (50 mM Tris-HCl pH 8.0, 300 mM NaCl, 10 mM imidazole, 10% (v/v) glycerol) and lysed by passage through a high-pressure homogenizer (ATS Engineering AH-2010) at −20°C. The lysate was treated with 0.1% (v/v) IGEPAL CA-630 (Sigma-Aldrich) and 0.05% (v/v) polyethylenimine (PEI) as previously described (Lu and Gong, 2013; Wu et al., 2020), and then centrifuged at 17, 000 rpm in an F21-8 × 50y rotor (Thermo Scientific) for 90 min to remove cell debris. The clarified lysate was loaded on to a HisTrap HP column (GE Healthcare). A stepwise wash with 25, 40, 50, and 60 mM imidazole was applied prior to the elution step with 300 mM imidazole. The pooled fractions were diluted with a low-salt Q buffer (25 mM Tris-HCl pH 8.5, 50 mM NaCl, 10% (v/v) glycerol, 0.1 mM EDTA) to reduce NaCl concentration to approximately 50 mM and then loaded onto a HiTrap Q HP column (GE Heathcare). The target proteins were eluted by a linear NaCl gradient to 1 M in 25 mM Tris-HCl pH 8.5, 10% (v/v) glycerol, 0.1 mM EDTA. The pooled fractions were concentrated and then loaded onto a Superdex 200 column (GE Healthcare) equilibrated with a GF buffer (for nsp12: 20 mM Tris-HCl pH 8.0, 4 mM $MgCl_2$, 400 mM NaCl, 10% (v/v) glycerol; for nsp7 and nsp8: NaCl concentration was reduced to 200 mM and glycerol was not included). The pooled fractions were concentrated to a final concentration of 10-30 mg/ml and stored as single-use aliquots at −80°C. The extinction coefficients for these proteins was calculated based on their sequences using the ExPAsy ProtParam (https://www.expasy.org/).

A pET26b-Ub-based plasmid containing the EV71 (strain HeN09-17/HeN/CHN2009) $3D^{pol}$ (RdRP) gene was used as the original cloning templates to construct the mutant plasmids according to previously described methods (Gohara et al., 1999; Papworth et al., 1996; Shu and Gong, 2016). Cell growth, IPTG induction, cell harvesting, cell lysis, protein purification, and protein storage were performed as described previously (Shi et al., 2020; Shu and Gong, 2016). DENV2 (strain TSV01) NS5 was prepared using a pET26b-based plasmid following previously decribed methods (Wu et al., 2020). The HCV (isolate BK) NS5B was prepared using a pET26b-based plasmid and *E. coli* Rosetta (DE3) strain. Protein purification and storage for HCV NS5B were performed as previously described in the JEV NS5 study (Lu and Gong, 2013), except that a 100 mM imidazole wash step was applied prior to the elution step of the Ni-affinity chromatography, and MES (pH 6.5) and Tris (pH 7.5) were used as the buffering agents for the cation-exchange and gel filtration columns, respectively. The yield is typically 3 mg of pure NS5B protein per liter of bacterial culture.

RNA preparation and RdRP catalytic complex assembly

RNA templates T33-1, T33-7, T33-8, T35, and T56 were prepared through a T7 RNA polymerase-*glmS* ribozyme-based method as described previously (Batey and Kieft, 2007). RNA primer P10 was purchased from Integrated DNA Technologies. P10 was annealed to T33-1/T33-7/T33-8/T35 and T56 at 1.1:1 and 3.1:1 molar ratios, respectively (Gong and Peersen, 2010). The T33-1- and T33-7-derived P14-containing catalytic complexes were assmebled and purified as described previously (Wang et al., 2020c). For T56-derived P14-containing catalytic complex assembly, a typical 1.5 mL reaction system containing 12 μM nsp12, 12 μM nsp7, 24 μM nsp8, 10 μM T56/P10 × 3, 300 μM CTP, 300 μM ATP in a reaction buffer of 50 mM HEPES (pH 7.0), 50 mM NaCl, 5 mM $MgCl_2$, 4 mM dithiothreitol (DTT) was incubated at 25°C for 120 min. The reaction mixture was loaded onto a MonoQ column (GE Healthcare) for complex purification. Unless otherwise indicated, catalytic complex samples were buffer exchanged to complex buffer (50 mM HEPES (pH 7.0), 100 mM NaCl, 4 mM $MgCl_2$, 4 mM DTT) and concentrated to at least 2 mg/ml for enzyme assays and about 5 mg/ml for cryo-EM data collection.

Cryo-EM Grid Preparation and Data Collection

300-mesh Quantifoil R0.6/1.0 grids (Quantifoil, Micro Tools GmbH, Germany) were glow-discharged using Solarus (Gatan) in H_2/O_2 atmosphere for 25 s. Then, 3 μL aliquots of protein-RNA complex were applied to the charged grids immediately after mixed with

0.025% (w/v) *n*-dodecyl-β-D-maltoside (DDM). In FEI Vitrobot III with chamber temperature at 8°C and humidity at 100%, solution-absorbed grids were blotted for 2.5 s with force 1 and transferred into pre-cooled liquid ethane. Images were collected on Titan Krios 300 keV electron microscope (Thermo Fisher scientific), equipped with K2 direct electron detector camera at EFTEM 165000 × with a calibrated super-resolution pixel size 0.82 Å/pixel. The exposure time was set to 5 s and total accumulated dose was set to 60 $e^-/Å^2$. All dose-fractioned images were automatically recorded using SerialEM (Mastronarde, 2005) with defocus ranging from 1.2 μm to 1.8 μm and 6,118 movies were recorded in tif format.

Cryo-EM Image Processing and structure determination

Motion-corrected and dose-weighted images were generated from raw movies using MotionCorr2 software (Zheng et al., 2017). In cryoSPARC (Punjani et al., 2017), image contrast transfer functions were calculated from patch CTF estimation and a total of 1,094,987 particles were automatically picked with PDB model 7C2K as the template (Wang et al., 2020c), and then extracted with 320 pixels. 620,118 particles were selected after two rounds of 2D classifications and 339,595 particles were converged into one complete protein-RNA complex class after *ab initio* and heterorefinement. This particle set generated a final resolution of 3.0 Å after homogeneous refinement and local refinement. In order to validate preferred orientation, local resolution estimation and 3DFSC were also calculated (Cardone et al., 2013; Tan et al., 2017).

To obtain the final model, the structure of SARS-CoV-2 RdRP pre-translocated catalytic complex (PDB: 7C2K) (Wang et al., 2020c) was first rigid-body fitted into the map using UCSF Chimera (Pettersen et al., 2004) and manually adjusted according to the cryo-EM map in COOT (Emsley et al., 2010). Main-chain backbone of the N-terminal region of the two nsp8s (residue 1-51) were built according to the structure of a replicating SARS-CoV-2 polymerase (Hillen et al., 2020) (PDB: 6YYT). Further real space refinement of the merged structure model was carried out in PHENIX (Adams et al., 2013).

Unless otherwise indicated, protein structure superimposition was done using the maximum likelihood-based structure superpositioning program THESEUS (Theobald and Wuttke, 2006).

In vitro primer-dependent RdRP assays for SARS-CoV-2 and other RNA viruses

For characterizing SOF-TP/T-1105-TP/RDV-TP (SeNTInall Bio Technologies) intervention, a typical 20-μl reaction mixture containing 6 μM nsp12, 6 μM nsp7, 12 μM nsp8, 300 μM NTP each, 4 μM T33-8/P10, T33-1/P10, or T35/P10 in a reaction buffer of 50 mM HEPES (pH 7.0), 5 mM $MgCl_2$, 4 mM DTT, 50 mM NaCl was incubated at 25°C for 5, 20, 60 min. The reaction was quenched with equal volume of stop solution (95% (v/v) formamide, 20 mM EDTA (pH 8.0), 0.02% (w/v) bromphenol blue). A DNA completely complementary to the RNA template was added to the quenched sample to help resolve the RNA product. The mixture was heated at 95°C for 45-60 s and slowly cooled to r.t. before denaturing polyacrylamide gel electrophoresis (PAGE) analysis.

To characterize T33-1- and T56-derived catalytic complex reactivity, GTP was provided at 100 μM to trigger the P14-to-P16 conversion at 4 or 25°C for 0 (quenched immediately after manual mixing), 0.5, 1, 2, 5, 10, 30 min. For stability characterization, NaCl was supplemented to reach a concentration of 200 mM and the mixture was incubated at 4 or 16°C for various periods (0-75 h), and then GTP was provided at 100 μM to trigger the P14-to-P16 conversion at 4°C for 5 min. The fraction of P16 intensity values was fitted to a single-exponential decay model to estimate the inactivation rate constant (k_{ina}) of the catalytic complex. For a better estimation of k_{ina}, the intensity of P14 failed to convert after 0 min incubation was used to adjust the P14 intensity (subtracted) measured from other incubation time points.

For RDV-TP incorporation with T33-7-derived catalytic complex, a typical 20 μL reaction mixture containing 100 μM GTP, 100 μM RDV-TP or ATP, and 4 μM catalytic complex in a reaction buffer of 50 mM HEPES (pH 7.0), 100 mM NaCl, 4 mM $MgCl_2$, 4 mM DTT was incubated at 6°C. For RDV-TP incorporation with T56-derived catalytic complex, a typical 20 μL reaction mixture containing 100 μM GTP, 100 μM RDV-TP or ATP, 100 μM UTP, and 4 μM catalytic complex in buffer 50 mM HEPES (pH 7.0), 100 mM NaCl, 4 mM $MgCl_2$, 4 mM DTT was incubated at 0°C (ice-water mixture).

For EV71 RdRP assays, a 20-μl reaction mixture containing 4 μM T33-1/P10 construct, 6 μM $3D^{pol}$, 30 mM NaCl, 50 mM KCl, 50 mM HEPES (pH 7.0), 5 mM $MgCl_2$, 5 mM TCEP was pre-incubated at 22.5°C for 15 min, Then 300 μM CTP, 300 μM ATP (or RDV-TP), various concentrations of GTP (20-300 μM) were provided to initiate the reaction. For DENV2 RdRP assays, a typical 20-μl reaction mixture containing 6 μM DENV2 NS5, 300 μM ATP or RDV-TP, 300 μM UTP, 4 μM T30/P2 construct in a reaction buffer of 50 mM Tris (pH 7.5), 5 mM $MgCl_2$, 5 mM DTT, 20 mM NaCl was incubated at 30°C for 15, 60, 120 min. The HCV RdRP assays are the same as the DENV2 assays except that 50 mM MES (pH 6.5) and 3 mM $MgCl_2$ were used in the reaction buffer and the incubation time points were for 5, 15, 60 min.

Unless otherwise indicated, gel electrophoresis and RNA visualization by Stains-All (Sigma-Aldrich) staining were performed as previously described (Wang et al., 2020c; Wu et al., 2020) and band intensity quantification was performed using ImageJ (https://imagej.nih.gov/ij).

QUANTIFICATION AND STATISTICAL ANALYSIS

Band intensity quantification was performed using ImageJ. All reported cryo-EM structure resolutions were based on gold-standard FSC 0.143 criteria (Rosenthal and Henderson, 2003).